CrystEngComm

Accepted Manuscript

ROYAL SOCIETY OF CHEMISTRY

www.rsc.org/crystengcomm

Fe_2O_3 Icositetrahedrons, Evolution and Their Comparative Photocatalytic Activities

Pengwei Li, [*] [a] Jianlong Ji, [a] Xiao Deng, [b] Anli Li, [a] Jie Hu, [a] Gang Li, [a] Wendong Zhang [a]

Abstract

Single crystal Fe_2O_3 icositetrahedrons have been synthesized by a facile hydrothermal systhesis method in the presence of dihydrogen phosphate ions. The icositetrahedron particles are of hexagonal shape and enclosed by 24 quadrilaterals. It could be seen as a particle with six equivalent {110} facets adding to the truncated hexagonal bipyramidal structure, that is, it is enclosed by six {110} planes, six {104} planes and twelve {113} planes. Dihydrogen phosphate ions play an important role in the formation of α-Fe_2O_3 icositetrahedron particles, because high concentration of $[H_2PO_4]^-$ drives the ferric oxide nanocrystals growth along [006] zone axis. Furthermore, the as-synthesized Fe_2O_3 icositetrahedron single crystals show comparative photocatalytic activities on the degradation of cationic dye Rhodamine B, which make them the promising candidates for catalysts and sensing materials.

Key words: Ferric oxide; Polyhedron; Crystal growth; Photocatalytic

* To whom correspondence should be addressed. E-mail: lipengwei@tyut.edu.cn.
[a] Micro-Nano System Research Center, College of Information Engineering, Taiyuan University of Technology, Taiyuan 030024, Shanxi, China
[b] College of Physics and Optoelectronics, Taiyuan University of Technology, Taiyuan 030024, Shanxi, China

1. Introduction

Structural and morphological control over inorganic crystals has recently attracted more and more attention because of the special size- and shape-dependent unique physical and chemistry properties.[1-4] Therefore, studies on the shape controllable synthesis of nanomaterials are of great interest and actively being pursued. In particular, many efforts have been devoted to a precise control of uniform polyhedral-shaped crystals,[5-9] due to their potential high percentage of exposed high-reactive crystal facets and the corresponding excellent properties in catalysis,[5-7] lithium ion batteries,[8] and surface-enhanced raman scattering,[9] etc. For instance, Tian et al. developed the tetrahexahedral Pt nanocrystals with 24 high-index facets exhibiting much enhanced (up to 400%) catalytic activities toward the electro-oxidations of formic acid and ethanol.[5] Wang et al. synthesized the polyhedral 50-facet Cu_2O microcrystals partially enclosed by {311} high-index planes, which shows enhanced catalytic CO oxidation activity.[6]

Hematite (α-Fe_2O_3), an n-type semiconductor (E_g = 2.1 eV), is the most thermodynamically stable phase of iron oxide. Many recent efforts have been directed toward the fabrication of nanostructural iron oxides to enhance their performance in currently existing applications. To date, well-defined nanostructures of iron oxides with different dimensionalities such as nanorods, nanorings, nanotubes, nanospindle, and nano-polyhedrons (cube, octahedral, hexagonal bipyramidal and octadecahedral nanostructures) have been obtained successfully by a series of solution-based routes.[10-20] As expected, these Fe_2O_3 nanostructures lead to interesting size and shape-dependent properties and a wide variety of potential applications, including catalysts,[10] gas sensors,[11,12] biosensors,[13] and electrode materials,[14,15] owing to its nontoxicity, low processing cost, and high resistance to corrosion. However, due to the similar surface energies of various low index facets of hematite, the order of stability of surfaces can be changed easily by preferential adsorption of ionic species or slight alterations to reaction conditions.[18] It still remains challenges to develop a facile and environmental friendly route to synthesize the polyhedral structure hematite

with more high-reactive crystal facets.

In this work, we report a hydrothermal process to the synthesis of single crystal Fe_2O_3 icositetrahedrons with 24 facets that show an enhanced specific photocatalytic rate toward Rhodamine B (RhB) degration due to the presence of unsaturated, high-reactive {104} facets.

2. Experiment Section

2.1 Materials preparation

All the reagents were purchased from Sinopharm Chemical Reagent Co. Ltd. In a typical procedure, an aqueous solution was first prepared by mixing 60 mL of deionized water (18 MΩ), 0.324 g ferric chloride hexahydrate (0.02 M) and 0.0019g sodium dihydrogen phosphate (0.2 mM) in a 100-mL flat-bottomed flask. The mixture was stirred with a magnetic blender for about 10 min and then transferred into a stainless-steel autoclave with a capacity of 100 mL, sealed and heated at 220 ºC for 5 h. When the reaction was completed, the autoclave was cooled to room temperature naturally. The brick red precipitate was centrifuged, washed several times with distilled water and absolute alcohol, and finally dried in a dry oven at 60 ºC for 5h for further characterizations. In this article, there are total four samples: Sample A, Sample B, Sample C and Sample D have been prepared, corresponding to different phosphate ions concentrations (0.1 mM, 0.2 mM, 0.3 mM and 0.4 mM, respectively).

2.2 Characterization

The crystal structures, morphologies, and chemical compositions of the as-prepared samples were studied using X-ray diffraction (XRD, X'Pert Pro MPD system, CuKα), scanning electron microscopy (SEM, Hitachi S-4800), transmission electron microscopy (TEM, JEOL 2100F, 200 kV). The surface areas of the catalysts were calculated by N_2 adsorption-desorption isotherms using a TriStar 3000 with the Brunauer-Emmett-Teller (BET) methods. For Zeta potential measurements, a commercial dynamic light scattering instrument (DLS, Malvern Nano zetasizer 90) has been chosen in this work. X-ray photo-electron spectroscope (XPS, ESCALAB 250XI) measurements were also carried out for the analysis of surface element

composition.

2.3 Photocatalytic properties

The photocatalytic activity of the as-prepared samples for the degradation of RhB in aqueous solution was evaluated by measuring the adsorbance of the irradiated solution, using a spectrophotometer (Shimadzu, 3100 UV-vis-NIR). Prior to irradiation, 10 mg of photocatalyst was mixed with RhB (50 mL, with a concentration of 0.02 mM) in a 100-mL flat bottom flask and then sonicated in a cool water bath for 10 min. Afterward, the suspension was magnetically stirred in the dark for 1 h to reach a relative adsorption-desorption equilibrium, followed by the addition of 0.3 mL of hydrogen peroxide solution (H_2O_2, 30 wt %). Then the beaker was exposed to visible light irradiation with maximum illumination time up to 4 hours. During the irradiation, the suspension was magnetically stirred by using a magnetic stirrer and the reaction temperature was kept at room temperature by using a water cooling system. The suspension was subsequently illuminated by a 300 W xenon lamp (the wavelength distributes from 400 nm to 800 nm) at a ca. 30 cm distance (the optical irradiance at the sample was about 30 mW cm^{-2}). A wave filter plate (λ >420 nm) was utilized to allow visible light to transmit. At given time intervals (0.5 h), about 4 mL aliquots were sampled and centrifuged to separate the catalyst. The dye concentration in the filtrate was analyzed by measuring the absorption intensity of RhB at 554 nm.

3. Results and discussion

The shape of the typical Fe_2O_3 icositetrahedrons was determined initially by SEM. An overview SEM image of the hematite nanoparticles with a growth concentration $[H_2PO_4]^-$ of 0.2 mM (Sample B) was shown in Fig.1 (a). The samples seemed as nanorices (105±3 nm in diameter and 160±10 nm in length) and were homogeneous in shape. In the final products, the yield of the Fe_2O_3 nanorices was larger than 95%, and the most other shapes were imperfect Fe_2O_3 nanorices or their agglomerations. Fig. 1 (b) shows a high-magnification SEM image of the Fe_2O_3 nanorices, from which we can see that the Fe_2O_3 nanorices have truncated short-rod structure. The top view figure (insert of Fig. 1b) of the end of typical nanorice gives more details of the

structure: hexagonal cylinder, pyramidal end and truncated feature. To sum up, it could be speculated that the as-prepared samples are hexagonal polyhedrons with 24 quadrilaterals for a particle, in other word, icositetrahedron, as shown in Fig. 1 (c). The purity and crystallinity of the typically synthesized product was determined by XRD (Fig. 1d). All peaks in the pattern can be perfectly indexed to rhombohedral hematite (α-Fe_2O_3, JCPDS 33-0664). No other phase was observed, indicating high phase purity.

TEM investigations give overall structural information of the synthesized samples (Fig. 2 and Fig. S1). Fig. 2(a) shows a bright field TEM image at low magnification which clearly reveals the truncated short-rod structure of the as-synthesized Fe_2O_3 icositetrahedrons. The crystallographic orientation of each exposed surface was determined through the analysis of diffraction and high resolution TEM (HRTEM) images (Fig. 2b-k). To assign the surface facets, the nanoparticles were tilted in TEM until the surface was parallel to the beam.[21] When the Fe_2O_3 icositetrahedron was tilted along the [2-10] direction (SAED, Fig. 2c), six side facets were parallel to the electron beam (Fig. 2b,c,f). The spacing of lattice planes parallel to the surface were measured to be 0.22 nm (Fig. 2d, HRTEM image of region '1' in Fig. 2b) and 0.25 nm (Fig. 2e, HRTEM image of region '2' in Fig. 2b), corresponding to α-Fe_2O_3 {113} plane and {110} plane distance, respectively. So, the exposed side planes could be indexed to four equivalent {113} facets and two {110} planes, respectively. Meanwhile, the 'zigzag' edge of the particle's HRTEM image (Fig. 2e) could also be assigned to the equivalent {113} or {110} planes. The 'zigzag' edge indicates that the side faces of the Fe_2O_3 nanocrystal were defective, or, wrinkled in surface. This would be the evidence for the crystal growth of Fe_2O_3 icositetrahedron along [006] zone axis. More detailed facets were labeled on its geometrical configuration figures (Fig. 2f).

When the particle was tilted clockwise 30º from [2-10] to [100] zone axis (Fig. 2g,h,k), two top surfaces have become parallel to the electron beam and can be indexed as the (0-14) planes from the SAED pattern (Fig. 2h). The HRTEM images (Fig. 2i and j) obtained from the white rectangles '3' and '4' in Fig. 2g showed a perfectly resolved lattice spacing of 0.27 nm, corresponding to hematite {104} planes,

and were consistent with the SAED pattern analysis (Fig. 2h).

It is well-known that the kinetic control of the monomer concentration and the crystal growth rate is the key factor to manipulate the particle size as well as material shapes initiated from the anisotropic growth.[22, 23] Phosphate ions, as we know, have been widely used as a shape controller to induce anisotropic growth of hematite nanocrystals.[3, 24, 25] In this work, concentration dependent experiments were performed to explore the influence of phosphate ions on the anisotropic growth of Fe_2O_3 icositetrahedrons (Fig. 3). When the usage of phosphate ions decreased (0.1 mM), the axial length of the nanocrystal shortened to 120±8 nm (Fig. 3a), the diminishing portion of which was mainly reflected in the length shorten of the icositetrahedron and the area decrease of the exposed {110} planes (Fig. S1). In another case, when a large quantity of $[H_2PO_4]^-$ (0.3 and 0.4 mM) was introduced, Fe_2O_3 icositetrahedrons with 190±15 nm and 240±18 nm axial length were obtained (Fig. 3c,d). With an increasing amount of phosphate ions, the morphologies of these particles changed continuously (Fig. 3e) with the aspect ratio, from 1.14 to 2.26 (Tab. 1). Which means that, the increasing amount of phosphate ions mainly driven the Fe_2O_3 icositetrahedrons growth along [006] zone axis. However, from the SEM images (Fig. 3c, d and Fig. S2), it could also be found that the Fe_2O_3 crystals grow imperfectly (especially the end of the crystals, vanished gradually) with the $[H_2PO_4]^-$ concentration becomes excessive. Perhaps, besides the functioning as a ligand, the phosphate also plays the role of etching agent.[25] The detailed mechanism still needs more in-depth study and further research will be undertaken.

On the basis of previous literature and our experimental results, a plausible action mechanism of phosphate ions on Fe_2O_3 icositetrahedrons growth was proposed.[23, 25-28] Firstly, the additive phosphate ions, with their strong affinity for Fe_2O_3 {110} planes,[3, 25] will act as a shape controller to induce anisotropic growth. The formation of Fe_2O_3 with $FeCl_3$ as source generally involves two reactions (1, 2) as follows:

$$Fe^{3+} + 3H_2O \leftrightarrow Fe(OH)_3 + 3H^+ \quad (1)$$

$$2Fe(OH)_3 \leftrightarrow Fe_2O_3 + 3H_2O \quad (2)$$

$$H_2PO_4^- \leftrightarrow HPO_4^{2-} + H^+ \quad (3)$$

$$Fe_2O_3 + 6H^+ \leftrightarrow 2Fe^{3+} + 3H_2O \quad (4)$$

When $[H_2PO_4]^-$ was added into the reaction, the faintly acid of the agent (reaction 3) will not only reduce the hydrolysis of Fe^{3+}, but also influence the dehydration of $Fe(OH)_3$. In addition, when $[H_2PO_4]^-$ was added excessively, it may probably etches the formed products (reaction 4). So the morphology evolution of Fe_2O_3 nano-icositetrahedrons should be a result of the changes of reaction rate caused by the addition of NaH_2PO_4.

To further investigate the delicate structure of icositetrahedrons, Figure 4a-c illustrates the atomic configurations model for one of the Fe_2O_3 single crystal icositetrahedrons, according to its rhombohedral structures. Figure 4b and c gave the atomic configurations along [2-10] and [100] zone axis, respectively. From both of them, it is clearly shown that oxygen atoms are the terminated atoms of the {006} facets of Fe_2O_3, which are positive with higher polar faces and more conducive to the absorption of Fe^{3+} cations and driven the growth of α-Fe_2O_3 on the initial crystal nuclei.[18, 29] Thus, fast growth occur on the [006] zone axis direction. Figure 4d-f displays the side view atomic configurations of the exposed crystal facets, {110}, {113} and {104} planes of Fe_2O_3 icositetrahedrons, respectively. It can be found that different crystal facets possess distinct surface atom structures: the {110} facets possess more Fe dangling bonds; [28] the {113} planes are nearly neutral; while, the {104} facets show the periodic characteristics of corrugated, with some unsaturated 'hot spot' (O dangling bonds) on them. These informations state that the as-synthesized Fe_2O_3 icositetrahedrons possess peculiar surface physical and chemical properties. At the same time, it also explains why the Fe_2O_3 icositetrahedrons corroded from the end of the crystal (dominated by {104} facets with more unsaturated 'hot spot'), [30, 31] with the amount of the $[H_2PO_4]^-$ was excess.

The optical properties of the as-prepared samples were investigated by a spectrophotometer (UV-vis-NIR). Figure 5(a) shows the absorption spectra for α-Fe_2O_3 icositetrahedrons with various axial lengths (120-240 nm, Samples from A to

D) in deionized water. All the four samples almost share the similar features of absorption, the broad band around 520 nm, which overlaps the absorption band with RhB (554 nm) and methyl orange (MO, 462 nm) dyes. In addition, the absorption edge exhibits systematic red shift (from about 700 nm to 1000 nm) with increasing the particle size (mainly about the axial length of the particle), and this was consistent with the former report. [19, 32] According to the interband transition formula in direct-gap semiconductor near the absorption edge, the absorption coefficient (α) and optical gap (E_g) obey the following equation: [33, 34]

$$(\alpha h\nu)^2 = A(h\nu - E_g) \qquad (5)$$

where A is restricted by the valence and conduction band of material and hν is the photon energy. Thus by linearly fitting on the absorption edge of the corresponding curve, the band gaps of the single crystal Fe_2O_3 icositetrahedrons (from Sample A to D) were obtained to be 2.01, 1.96, 1.90 and 1.55 eV, respectively (upper inset of Fig. 5a). The difference of which, may be ascribed to the size effect of the α-Fe_2O_3 nanoparticles.

Figure 5(b) shows the specific surface area (SSA) and Zeta potential (in neutral water solution, PH=7) of different samples. With the axial length of the Fe_2O_3 icositetrahedrons increase (from Sample A to D), the SSA of the sample decreased from 9.8 to 7.5 m^2g^{-1}; at the same time, the Zeta potential of the sample also decreased from -4.3 to -34.6 mV, that is, the material's electronegativity enhanced. Rule out the influence of surface area of the samples, the electronegativity enhancement could only be attributed to the polarity of the exposed crystal facets, especially here, only relevant to the exposed {110} facets, for that only the {110} facets' surface proportion increased with the axial length of the Fe_2O_3 icositetrahedron increased. This result could be well explained by the atom configurations characteristics (possess more Fe dangling bonds, which could adsorb anions in solution and make the particle show negative Zeta potential) of the {110} facets. [35]

Surface element composition measurements of the samples were carried out using an XPS setup (Fig. 5c). The O 1s XPS spectra were deconvoluted by mixed

Gaussian-Lorentzian functions after a Shirley background subtraction. [36] The O 1s XPS spectra were fit with three peaks corresponding to oxide (Ox, 530 eV), adsorbed OH groups (531.5 eV), and adsorbed H_2O molecules (533.2 eV). In the peak fitting, each peak had four fitting parameters: peak position, full width at half-maximum (fwhm), Lorentzian-Gaussian (L/G) mixing ratio, and intensity. Three parameters (position, fwhm, and L/G ratio) for each component were constrained to be constant. In the present study, as will be shown below, the peak intensity of the adsorbed OH groups increased from sample A to D.

Figure 5(d) shows the changes of the RhB relative concentrations (C/C_0) as a function of irradiation time, where C is the concentration of RhB at the irradiation time t and C_0 is the initial concentration. For comparison, the photodegradation of RhB only with H_2O_2 (without Fe_2O_3 catalyst) has also been performed and the result shows that the self-degradation of RhB is almost negligible. When α-Fe_2O_3 nanoparticles are used under the same conditions, the photodegradation rates of RhB are significantly increased. It is supposed that the structural Fe^{3+} plays a key role in heterogeneous photo-Fenton reaction via the redox cycle between Fe^{3+} to Fe^{2+} to generate hydroxyl radicals. [37, 38] Simultaneously, it could be easily found that the smaller the samples are the better adsorption capacity (dark process) and more superior photocatalytic activities (4h photodegradation process) the samples possessed (Fig. S3, Tab. 1). The sequence of the adsorption capacity and photocatalytic activities of different length Fe_2O_3 icositetrahedrons is as follows: Sample A > Sample B > Sample C > Sample D. Similar things could also be found on the MO degradation (Fig. S4). Generally, this phenomenon would be attributing to the lager SSA of the smaller nanoparticles, [27] which has also been confirmed by our experiment (Tab. 1), that the SSA dominated the photocatalytic activities of the proposed Fe_2O_3 icositetrahedrons.

4. Conclusions

In summary, α-Fe_2O_3 nanoparticles with similar icositetrahedron structure but different axial lengths have been synthesized by a facile hydrothermal method.

Phosphate ions were speculated capping to Fe_2O_3 {110} facets, and driving the anisotropic growth of hematite along the [006] zone axis. Meanwhile, it acts an important role to controlled release the Fe^{3+} cations and leading to the Fe_2O_3 polyhedrons' evolution. Four samples (Sample A to D) have been prepared and evaluated as photocatalysts for the degradation of dye molecules. The photodegradation tests show that the SSA dominated the photocatalytic activities of the proposed Fe_2O_3 icositetrahedrons.

Acknowledgements

This work was supported by National Natural Science Foundation of China (Grant Nos. 51205276, 51205275, 51205274, 51205273 and 61474079), China Postdoctoral Science Foundation (Grant Nos. 20110491629 and 2013T60268), Shanxi Province Science Foundation for Youths (Grant Nos. 2012021021-5 and 2013021017-1), and Shanxi Province Foundation for Returness (Grant No. 2013-036).

References

1 S. Helmi, C. Ziegler, D. J. Kauert and R. Seidel, *Nano Letters*, 2014, **14**, 6693-6698.

2 M. Q. Lu, S. K. Yang, Y. P. Ho, C. L. Grigsby, K. W. Leong and T. J. Huang, *Acs Nano*, 2014, **8**, 10026-10034.

3 H. F. Liang, X. Xu, W. Chen, B. B. Xu and Z. C. Wang, *Crystengcomm*, 2014, **16**, 959-963.

4 X. L. Mou, X. J. Wei, Y. Li and W. J. Shen, *Crystengcomm*, 2012, **14**, 5107-5120.

5 N. Tian, Z. Zhou, S. Sun, Y. Ding and Z. Wang, *Science*, 2007, **316**, 732-735.

6 M. Leng, M. Z. Liu, Y. B. Zhang, Z. Q. Wang, C. Yu, X. G. Yang, H. J. Zhang and C. Wang, *Journal of the American Chemical Society*, 2010, **132**, 17084-17087.

7 S. I. Choi, S. F. Xie, M. H. Shao, J. H. Odell, N. Lu, H. C. Peng, L. Protsailo, S. Guerrero, J. H. Park, X. H. Xia, J. G. Wang, M. J. Kim and Y. N. Xia, *Nano Letters*, 2013, **13**, 3420-3425.

8 S. Z. Huang, J. Jin, Y. Cai, Y. Li, H. Y. Tan, H. E. Wang, G. Van Tendeloo and B. L. Su, *Nanoscale*, 2014, **6**, 6819-6827.

9 Y. J. Liu, S. Pedireddy, Y. H. Lee, R. S. Hegde, W. W. Tjiu, Y. Cui and X. Y. Ling, *Small*, 2014, **10**, 4940-4950.

10 Y. Jiao, Y. Liu, F. Y. Qu and X. Wu, *Crystengcomm*, 2014, **16**, 575-580.

11 P. Sun, C. Wang, X. Zhou, P. F. Cheng, K. Shimanoe, G. Y. Lu and N. Yamazoe, *Sensors and Actuators B-Chemical*, 2014, **193**, 616-622.

12 J. M. Ma, L. Mei, Y. J. Chen, Q. H. Li, T. H. Wang, Z. Xu, X. C. Duan and W. J. Zheng, *Nanoscale*, 2013, **5**, 895-898.

13 J. P. Wang, H. Gao, F. L. Sun, Q. Hao and C. X. Xu, *Biosensors & Bioelectronics*, 2013, **42**, 550-555.

14 J. M. Jeong, B. G. Choi, S. C. Lee, K. G. Lee, S. J. Chang, Y. K. Han, Y. B. Lee, H. U. Lee, S. Kwon, G. Lee, C. S. Lee and Y. S. Huh, *Advanced Materials*, 2013, **25**, 6250-6255.

15 X. Xu, R. Cao, S. Jeong and J. Cho, *Nano Letters*, 2012, **12**, 4988-4991.

16 B. L. Lv, Z. Y. Liu, H. Tian, Y. Xu, D. Wu and Y. H. Sun, *Advanced Functional Materials*, 2010, **20**, 3987-3996.

17 W. F. Tan, Y. T. Yu, M. X. Wang, F. Liu and L. K. Koopal, *Crystal Growth & Design*, 2014, **14**, 157-164.

18 M. Lin, L. Tng, T. Y. Lim, M. Choo, J. Zhang, H. R. Tan and S. Q. Bai, *Journal of Physical Chemistry C*, 2014, **118**, 10903-10910.

19 J. B. Lian, X. C. Duan, J. M. Ma, P. Peng, T. I. Kim and W. J. Zheng, *Acs Nano*, 2009, **3**, 3749-3761.

20 J. S. Chen, T. Zhu, C. M. Li and X. W. Lou, *Angewandte Chemie-International Edition*, 2011, **50**, 650.

21 M. Lin, H. R. Tan, J. P. Y. Tan and S. Q. Bai, *Journal of Physical Chemistry C*, 2013, **117**, 11242-11250.

22 X. G. Peng, L. Manna, W. D. Yang, J. Wickham, E. Scher, A. Kadavanich and A. P. Alivisatos, *Nature*, 2000, **404**, 59-61.

23 W. Liu, N. Wang, R. Wang, S. Kumar, G. S. Duesberg, H. Zhang and K. Sun, *Nano Letters*, 2011, **11**, 2983-2988.

24 M. Ozaki, S. Kratohvil, and E. Matijevic, *Journal of Colloid and Interface Science*, 1984, **102**, 146-149.

25 C. J. Jia, L. D. Sun, F. Luo, X. D. Han, L. J. Heyderman, Z. G. Yan, C. H. Yan, K. Zheng, Z. Zhang, M. Takano, N. Hayashi, M. Eltschka, M. Klaui, U. Rudiger, T. Kasama, L. Cervera-Gontard, R. E. Dunin-Borkowski, G. Tzvetkov and J. Raabe, *Journal of the American Chemical Society*, 2008, **130**, 16968-16977.

26 F. Lu, W. P. Cai and Y. G. Zhang, *Advanced Functional Materials*, 2008, **18**, 1047-1056.

27 H. F. Liang, W. Chen, X. D. Jiang, X. Xu, B. B. Xu and Z. C. Wang, *Journal of Materials Chemistry A*, 2014, **2**, 4340-4346.

28 Y. B. Zhao, F. Pan, H. Li, T. C. Niu, G. Q. Xu and W. Chen, *Journal of Materials Chemistry A*, 2013, **1**, 7242.

29 R. M. Cornell, U. Schwertmann, *The Iron Oxides: Structure, Properties, Reactions, Occurrences and Uses*, Wiley-VCH Weinheim, 2003.

30 Y. Shang, D. Sun, Y. M. Shao, D. F. Zhang, L. Guo and S. H. Yang, *Chemistry-a European Journal*, 2012, **18**, 14261-14266.

31 J. S. Chen, T. Zhu, X. H. Yang, H. G. Yang and X. W. Lou, *Journal of the American*

Chemical Society, 2010, **132**, 13162.

32 C. C. Chang, H. L. Wu, C. H. Kuo and M. H. Huang, *Chemistry of Materials*, 2008, **20**, 7570.

33 W. Liu, R. M. Wang and N. Wang, *Applied Physics Letters*, 2010, **97**, 041916.

34 G. X. Wang, X. L. Gou, J. Horvat and J. Park, *Journal of Physical Chemistry C*, 2008, **112**, 15220.

35 Ryan J. Kershner, Joseph W. Bullard and M. J. Cima, *Langmuir*, 2004, **20**, 4101-4108.

36 S. Yamamoto, T. Kendelewicz, J. T. Newberg, G. Ketteler, D. E. Starr, E. R. Mysak, K. J. Andersson, H. Ogasawara, H. Bluhm, M. Salmeron, G. E. Brown and A. Nilsson, *Journal of Physical Chemistry C*, 2010, **114**, 2256.

37 M. M. Cheng, W. J. Song, W. H. Ma, C. C. Chen, J. C. Zhao, J. Lin and H. Y. Zhu, *Applied Catalysis B-Environmental*, 2008, **77**, 355.

38 W. P. Du, Q. Sun, X. J. Lv and Y. M. Xu, *Catalysis Communications*, 2009, **10**, 1854.

Tables

Table 1. Sample parameters, reaction rate constants of RhB and MO degradation on iron oxides.

Samples	A	B	C	D
Diameter (nm)	105±4	105±3	104±2	106±3
Length (nm)	120±8	160±10	190±15	240±18
Aspect ratio	1.14	1.52	1.83	2.26
Surface area ($m^2 g^{-1}$)	9.8	9.3	8.4	7.5
Zeta potential (mV)	-4.3	-13.1	-29.7	-34.6
Reaction rate constant k_1 (h^{-1})	0.1668	0.1545	0.1369	0.1197
Reaction rate constant k_2 (h^{-1})	0.0529	0.0393	0.0275	0.0246

Where, 'k_1' represents the reaction rate constant of RhB degradation and 'k_2' represents the reaction rate constant of MO degradation.

Figure Captions

Figure 1. SEM images (a, b), geometrical configuration (c) and XRD pattern (d) for typical α-Fe_2O_3 icositetrahedrons synthesized at the $[H_2PO_4]^-$ concentration of about 0.2 mM (Sample B).

Figure 2. Typical morphology and structure of α-Fe_2O_3 icositetrahedrons. (a) bright field TEM image; (b-f) TEM image, corresponding SAED pattern, HRTEM images and geometrical configuration pattern showing the {113} and {110}surfaces parallel to the electron beam; (g-k) TEM image, corresponding diffraction pattern, HRTEM images and geometrical configuration pattern showing the {104} surfaces parallel to the electron beam when the same particle was tilted clockwise 30°.

Figure 3. (a-d) SEM images of shape evolution of α-Fe_2O_3 icositetrahedrons as a function of $[H_2PO_4]^-$ concentration: (a) 0.1, (b) 0.2, (c) 0.3 and (d) 0.4 mM, respectively; (e) Schematic diagram showing the axial growth of Fe_2O_3 icositetrahedron with the $[H_2PO_4]^-$ concentration increasing.

Figure 4. (a) Typical geometrical configuration of a Fe_2O_3 icositetrahedron paticle; (b, c) The atomic configurations of a Fe_2O_3 icositetrahedron paticle along [2-10] and [100] zone axis, respectively; (d-f) Side-view atomic configuration of the exposed crystal facets for Fe_2O_3 icositetrahedrons, {110}, {113} and {104}.

Figure 5. The optical properties of the as-prepared samples: (a) Absorption spectra for α-Fe_2O_3 icositetrahedrons with various axial lengths (Samples from A to D), the inset above shows linear fits (dashed lines) of the $(\alpha h\nu)^2$-hν curves calculated from the

absorption spectra; (b) The specific surface area (SSA) and Zeta potential (in neutral water solution, PH=7) of different samples from A to D; (c) O 1s XPS spectra of samples from A to D, the experimental data are shown as solid black lines and the results of the peak fitting are shown as short dash. (d) RhB concentration changes as a function of visible light irradiation time using different catalysts.

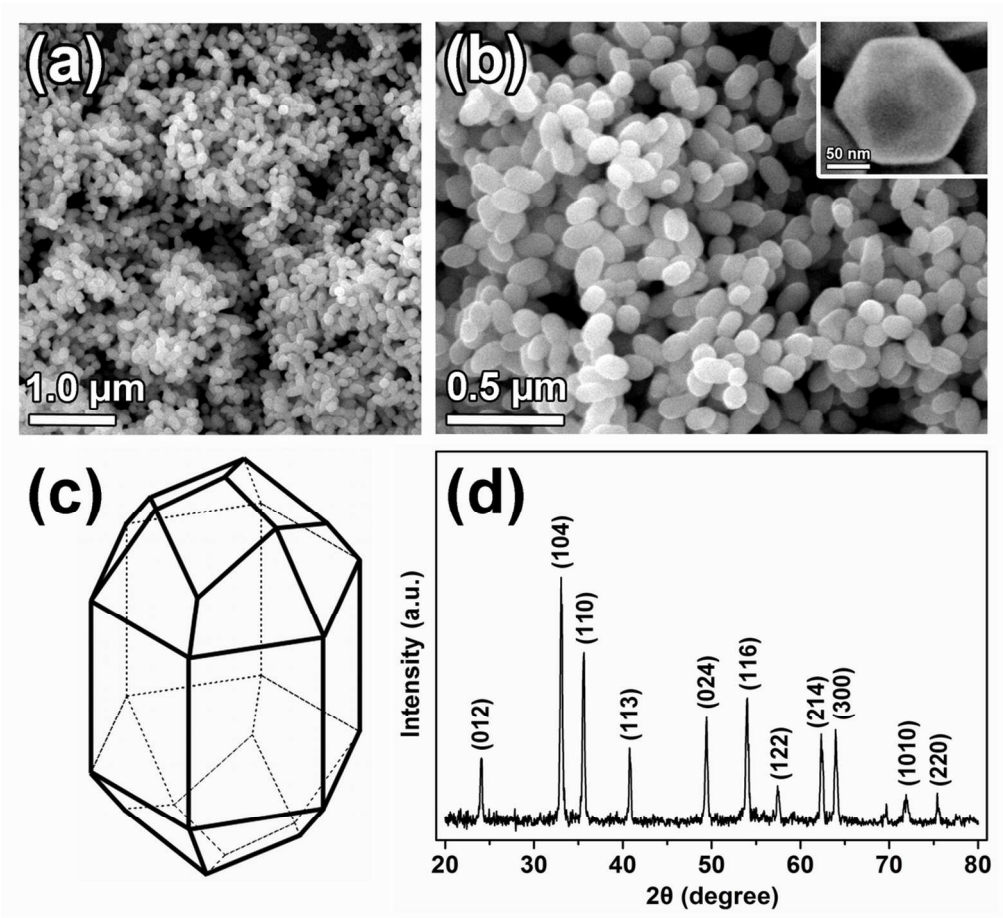

Figure 1. SEM images (a, b), geometrical configuration (c) and XRD pattern (d) for typical α-Fe2O3 icositetrahedrons synthesized at the [H2PO4]- concentration of about 0.2 mM (Sample B).
451x412mm (72 x 72 DPI)

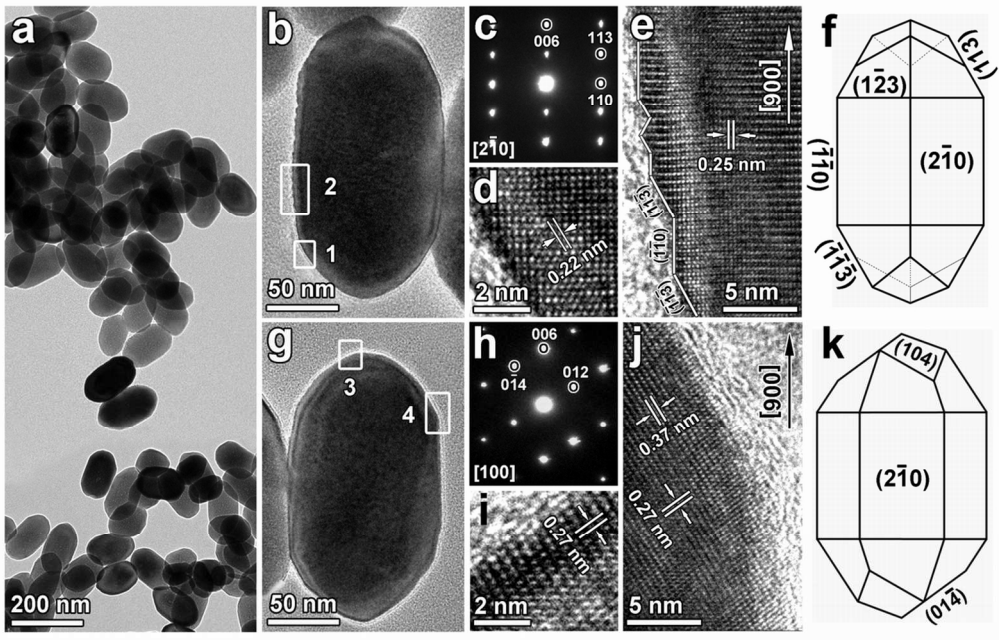

Figure 2. Typical morphology and structure of α-Fe2O3 icositetrahedrons. (a) bright field TEM image; (b-f) TEM image, corresponding SAED pattern, HRTEM images and geometrical configuration pattern showing the {113} and {110}surfaces parallel to the electron beam; (g-k) TEM image, corresponding diffraction pattern, HRTEM images and geometrical configuration pattern showing the {104} surfaces parallel to the electron beam when the same particle was tilted clockwise 30°.
451x289mm (72 x 72 DPI)

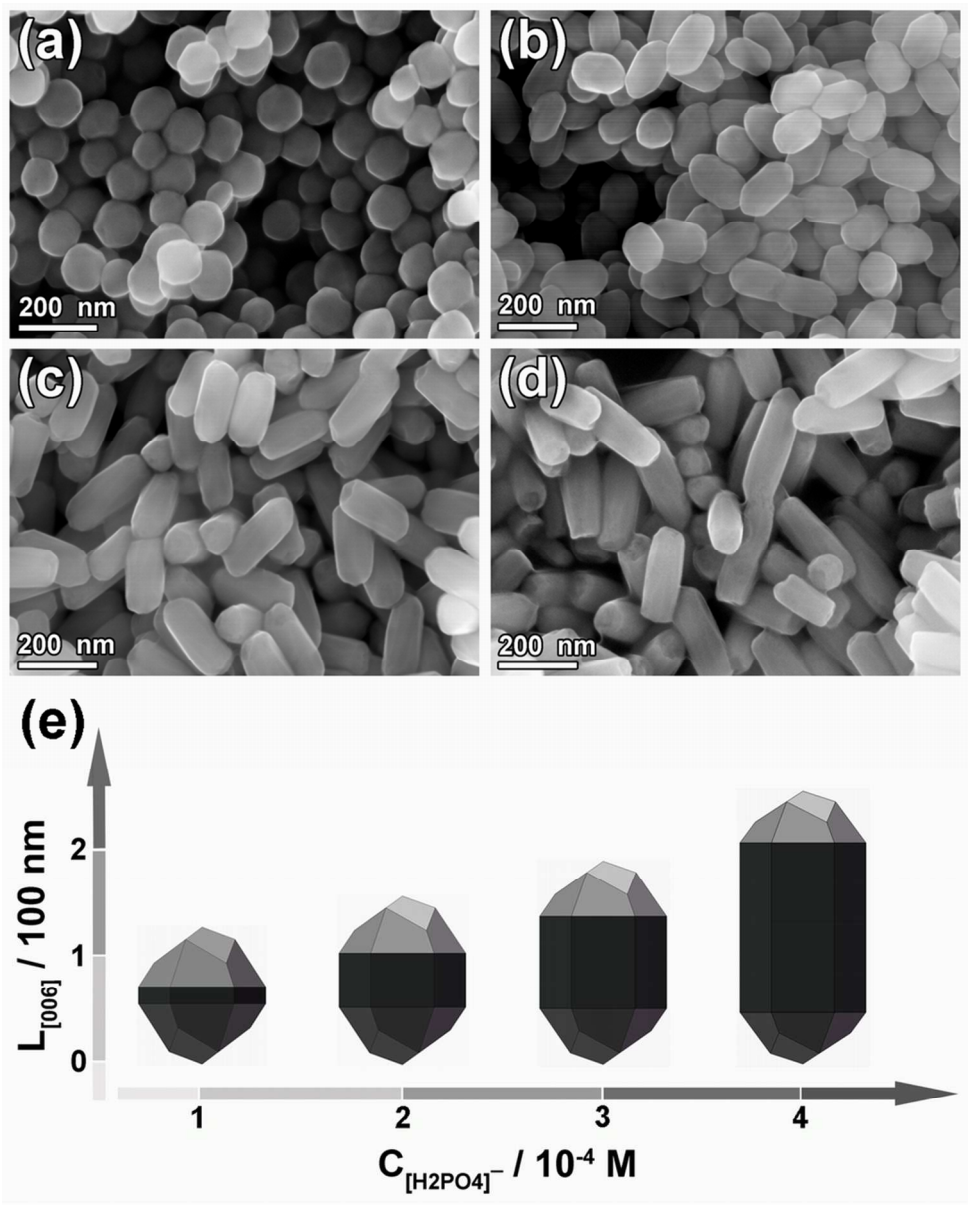

Figure 3. (a-d) SEM images of shape evolution of α-Fe2O3 icositetrahedrons as a function of [H2PO4]- concentration: (a) 0.1, (b) 0.2, (c) 0.3 and (d) 0.4 mM, respectively; (e) Schematic diagram showing the axial growth of Fe2O3 icositetrahedron with the [H2PO4]- concentration increasing.
363x451mm (72 x 72 DPI)

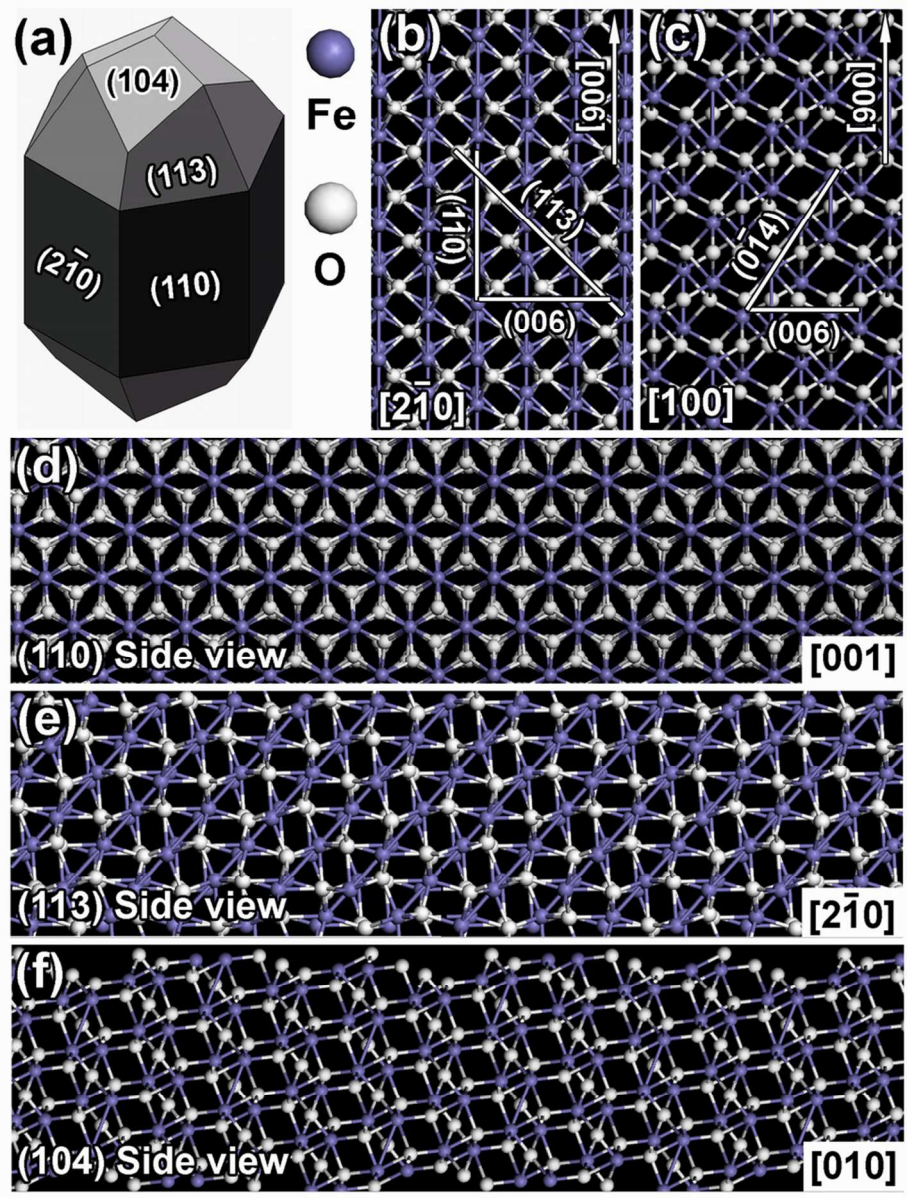

Figure 4. (a) Typical geometrical configuration of a Fe2O3 icositetrahedron paticle; (b, c) The atomic configurations of a Fe2O3 icositetrahedron paticle along [2-10] and [100] zone axis, respectively; (d-f) Side-view atomic configuration of the exposed crystal facets for Fe2O3 icositetrahedrons, {110}, {113} and {104}.
343x451mm (72 x 72 DPI)

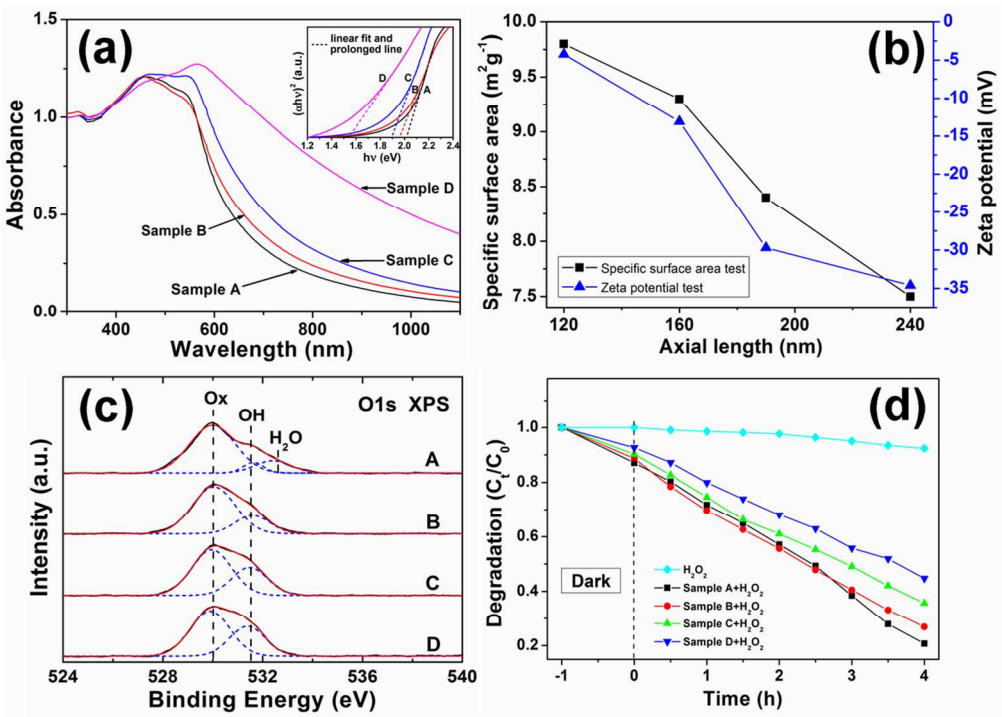

Figure 5. The optical properties of the as-prepared samples: (a) Absorption spectra for α-Fe2O3 icositetrahedrons with various axial lengths (Samples from A to D), the inset above shows linear fits (dashed lines) of the (αhν)2-hν curves calculated from the absorption spectra; (b) The specific surface area (SSA) and Zeta potential (in neutral water solution, PH=7) of different samples from A to D; (c) O 1s XPS spectra of samples from A to D, the experimental data are shown as solid black lines and the results of the peak fitting are shown as short dash. (d) RhB concentration changes as a function of visible light irradiation time using different catalysts.
451x321mm (72 x 72 DPI)

"Table of Contents" Graphic:

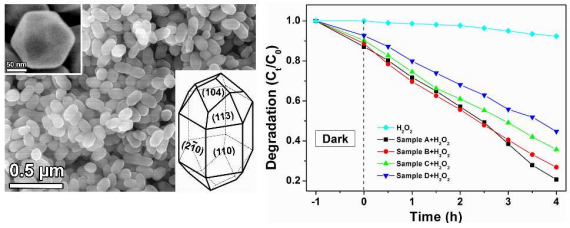

Fe_2O_3 Icositetrahedrons, Controllable synthesis and Their Comparative Photocatalytic Activities